Interplay of Homogeneous Reactions, Mass Transport, and Kinetics in Determining Selectivity of the Reduction of CO2 on Gold Electrodes

Benjamin A Zhang, Tuncay Ozel, Joseph S Elias, Cyrille Costentin, Daniel G Nocera

ACS central science

Research Article

Cite This: ACS Cent. Sci. 2019, 5, 1097−1105

http://pubs.acs.org/journal/acscii

Interplay of Homogeneous Reactions, Mass Transport, and Kinetics in Determining Selectivity of the Reduction of CO_2 on Gold Electrodes

Benjamin A. Zhang,[†] Tuncay Ozel,[†] Joseph S. Elias,[†] Cyrille Costentin,*[,†,‡] and Daniel G. Nocera*[,†]

[†]Department of Chemistry and Chemical Biology, Harvard University, 12 Oxford Street, Cambridge, Massachusetts 02138, United States

[‡]Laboratoire d'Electrochimie Moléculaire, Unité Mixte de Recherche Université, CNRS No. 7591, Bâtiment Lavoisier, Université Paris Diderot, Sorbonne Paris Cité, 15 rue Jean de Baïf, 75205 Paris Cedex 13, France

Supporting Information

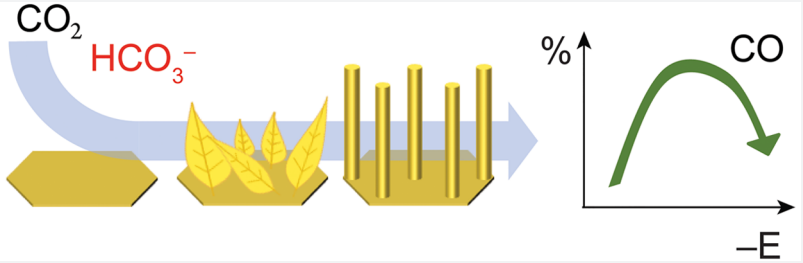

ABSTRACT: Gold electrocatalysts have been a research focus due to their ability to reduce CO_2 into CO, a feedstock for further conversion. Many methods have been employed to modulate CO_2 reduction (CDR) vs hydrogen evolution reaction (HER) selectivity on gold electrodes such as nano-/mesostructuring and crystal faceting control. Herein we show that gold surfaces with very different morphologies (planar, leaves, and wires) lead to similar bell-shaped CO faradaic efficiency as a function of applied potential. At low overpotential ($E > -0.85$ V vs standard hydrogen electrode (SHE)), HER is dominant via a potential quasi-independent rate that we attribute to a rate limiting process of surface dissociation of competent proton donors. As overpotential is increased, CO faradaic efficiency reaches a maximal value (near 90%) because CO production is controlled by an electron transfer rate that increases with potential, whereas HER remains almost potential independent. At high overpotential ($E < -1.2$ V vs SHE), CO faradaic efficiency decreases due to the concurrent rise of HER via bicarbonate direct reduction and leveling off of CDR as CO_2 replenishment at the catalyst surface is limited by mass transport and homogeneous coupled reactions. Importantly, the analysis shows that recent attempts to overcome mass transport limitations with gas diffusion electrodes confront low carbon mass balance owing to the prominence of homogeneous reactions coupled to CDR. The comprehensive kinetics analysis of the factors defining CDR vs HER on gold electrodes developed here provides an activation-driving force relationship over a large potential window and informs on the design of conditions to achieve desirable high current densities for CO_2 to CO conversion while maintaining high selectivity.

INTRODUCTION

An ample supply of solar energy to meet a drastically growing energy demand does so intermittently due to the diurnal solar cycle and fluctuations in photon flux.[1−4] A promising strategy to compensate for such intermittent availability is to convert solar energy to carbon neutral fuels in a sustainable and scalable manner, thus allowing solar energy to be harnessed in chemical bonds.[1,5] To this end, CO_2 reduction (CDR) to produce CO is an attractive strategy when coupled to the production of liquid fuels by syngas processing.[6] Whereas molecular electrocatalysts have been developed for CDR,[7] leading to efficient and selective production of CO[8] or formate,[9] the immobilization of the catalyst at the electrode surface may require additional tedious chemical synthetic steps, and turnover numbers usually remain below a few thousand.[10] Consequently, considerable effort has been devoted to developing heterogeneous electrocatalysts for CDR with the aim of improving turnover frequency and number at low overpotential.[11−18] Because CDR embodies a $2e^- \mid 2H^+$ process, catalyst development confronts the challenge of circumventing the competing hydrogen evolution reaction (HER). It has been generally recognized that nanostructuring gold electrodes can be effective in suppressing HER[19−25] and consequently promote CDR with high selectivity, though there is a lack of consensus in the reaction mechanism[26−29] and unsolved issues persist.[30]

A thorough analysis of parameters controlling electrocatalytic CDR is complex because it requires considerations of the kinetics of CDR and competing reactions (such as

Received: March 25, 2019
Published: June 10, 2019

DOI: 10.1021/acscentsci.9b00302
ACS Cent. Sci. 2019, 5, 1097−1105

HER), mass transport of species, and homogeneous reactions (see Table 1) that can alter the concentration of species in solution.[31] Kinetic rate laws for CDR and HER have been extracted from current density and the faradaic efficiency for CO (FE(CO)), but such rate laws have been constructed without considerations of mass transport and homogeneous reactions by examining CDR over a range of low overpotential.[26] When a wider potential range is examined, where mass transport and homogeneous reactions must be considered owing to higher current densities, rate laws have not been extracted from experimental data.[32] As high current densities are desirable for practically implementing CDR, the development of a comprehensive kinetics model for CDR over a wide potential range, where mass transport is operative and local concentration of substrates are affected by homogeneous reactions, will be beneficial as a guidepost to catalyst design.

Table 1. Homogeneous Reactions

reaction	K	k_f[a]
Hydration Reactions[c]		
$CO_2 + H_2O \rightleftharpoons H_2CO_3$	1.7×10^{-3}	0.03[a,d]
$CO_2 + HO^- \rightleftharpoons HCO_3^-$	4.27×10^{7}	2.2×10^{3}[b,e]
Acid−Base Reactions[c]		
$H_2CO_3 + H_2O \rightleftharpoons H_3O^+ + HCO_3^-$	2.51×10^{-4}	2.51×10^{6}[a]
$HCO_3^- + H_2O \rightleftharpoons H_3O^+ + CO_3^{2-}$	4.8×10^{-11}	0.48[a]
$HCO_3^- + HCO_3^- \rightleftharpoons H_2CO_3 + CO_3^{2-}$	1.9×10^{-7}	1.9×10^{3}[b]
$H_2CO_3 + OH^- \rightleftharpoons HCO_3^- + H_2O$	2.5×10^{10}	10^{10}[b]
$HCO_3^- + OH^- \rightleftharpoons CO_3^{2-} + H_2O$	4.8×10^{3}	10^{8}[b]
$2\ H_2O \rightleftharpoons H_3O^+ + OH^-$	10^{-14}	10^{-4}[b]

[a]In s^{-1}. [b]In $M^{-1}\ s^{-1}$. [c]Bulk concentrations of species in 0.1 M $NaHCO_3$ solution under a CO_2 atmosphere: $[CO_2]$ = 0.038 M; $[H_2CO_3]$ 6.5×10^{-5} M; $[HCO_3^-]$ = 0.1 M; $[CO_3^{2-}] = 2.9 \times 10^{-5}$ M. [d]Ref 33. [e]Ref 34.

To provide such a comprehensive kinetics model, we analyze CDR on different gold electrode morphologies (planar, leaf, and wire) in CO_2 saturated water in the presence of sodium bicarbonate ($NaHCO_3$) buffer. Our analysis produces an activation-driving force relationship for CDR on gold over a wide applied potential range, revealing that the catalyst's intrinsic CDR activity deviates from that predicted by Volmer behavior, and thus rate constants measured at low overpotential cannot simply be extrapolated to predict catalyst behavior at high overpotential.

Our results also are consequential to the practical application of CDR, for which catalysts displaying high FE(CO) are desired at high current densities while maintaining a low operating overpotential. We show that gold surfaces with very different structures exhibit a similar bell-shaped trend in FE(CO), with CDR at high overpotentials being suppressed owing to the onset of mass transport limitations and substrate consumption by the homogeneous reactions listed in Table 1. Therefore, neither increasing the surface area of a catalyst or increasing the applied overpotential will result in high FE(CO) at high current densities. Attempts to alleviate the limitations of mass transport have utilized gas diffusion electrodes (GDE). However, we show from our kinetics analysis that the role of homogeneous reactions greatly affects the overall mass balance of carbon in the CDR reaction.

RESULTS

Three gold electrodes with different morphologies but identical projected (geometric) surface areas (S_{geom} = 1.53 cm^2) were prepared (see Supporting Information for details): a flat gold film was obtained by gold evaporation; dendritic gold nanoleaves were obtained by electrodeposition; and polycrystalline gold nanowire arrays were obtained by electrodeposition of a gold layer of 25 nm on a prefabricated silicon nanowire array electrode, as we have recently described with our new method to conformally coat nanowires.[35] The three

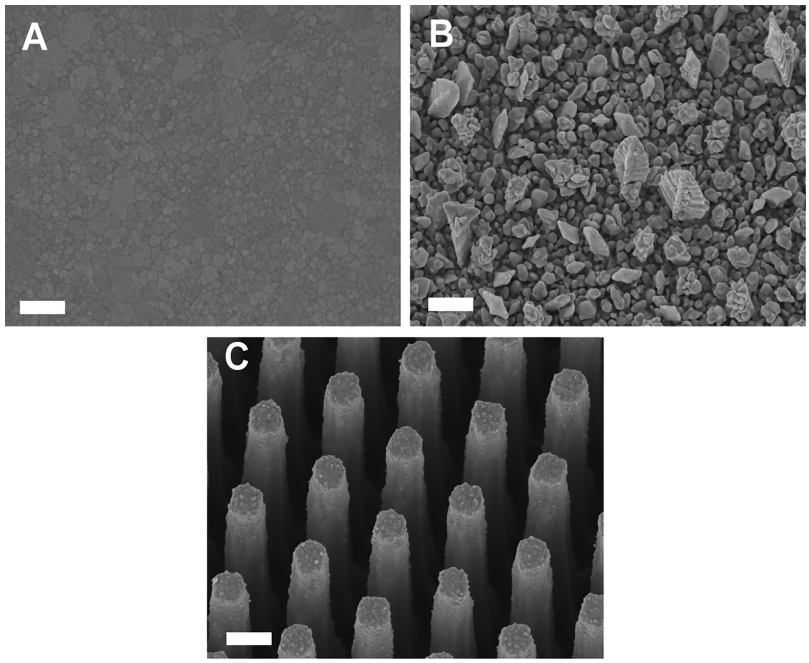

Figure 1. SEM image of (A) evaporated gold film, (B) electrodeposited gold leaf, and (C) electrodeposited gold nanowire array electrodes at 50k× magnification. Scale bar is 500 nm.

DOI: 10.1021/acscentsci.9b00302
ACS Cent. Sci. 2019, 5, 1097−1105

electrodes are referred herein as the *film electrode*, *leaf electrode*, and *wire electrode*. Scanning electron microscope (SEM) images of the three electrode arrays are shown in Figure 1. The electroactive surface area (S_{elec}) of each electrode was determined by both gold oxide dissolution and copper underpotential deposition (Figure S1). Referenced to a film electrode roughness factor ($R_f = S_{elec}/S_{geom}$) equal to 1, we obtain a leaf and wire electrode roughness factor of 4.37 and 15.44, respectively.

Potentiostatic measurements were conducted on each electrode in the range of −0.7 to −1.5 (or −1.8) V vs standard hydrogen electrode (SHE) using a custom designed two-compartment electrochemical cell (Figure S2). The electrolyte was 0.1 M $NaHCO_3$ and 0.5 M $NaClO_4$. During experiments, the solution was stirred, and a constant flow of CO_2 was delivered to the cathodic compartment and the exiting gas flowed directly to a gas chromatograph to quantify H_2 and CO production. No significant electrode deactivation over the course of electrolysis was observed due to poisoning or accumulation of adsorbed CO (Figures S3 and S4) (see Supporting Information for details), consistent with findings that adsorbed spectator CO species do not affect CDR.[26] The $H_2CO_3/HCO_3^-/CO_2$ solution is the standard buffer system for electrochemical CO_2 reduction, as the addition of conventional buffers such as $H_2PO_4^-/HPO_4^{2-}$ result in increased faradaic efficiency and partial current density for HER due to increased proton donor concentration (Figure S5). The high concentration of $NaClO_4$ as a supporting electrolyte minimized the participation of substrate (CO_2) and cosubstrate (HCO_3^-) in migration and double layer processes. Diffusion and convection are therefore the only modes of mass transport for electroactive carbonated species. Assuming planar linear diffusion, the thickness of the constant diffusion layer (δ) was evaluated as ca. 190 μm (Figure S6) (details of the determination are given in the Supporting Information).

Partial current densities (j, normalized by projected geometric surface area) for CO and H_2 production on each electrode are reported in Figure 2A–C. No products other than CO and H_2 were detected in significant amounts. Measurements at low overpotential exhibited a larger error due to the low current and therefore low gas concentration for quantification by gas chromatograph. We note that any type of mesostructuring, in comparison to a flat electrode, gives rise to an earlier potential onset for CO generation as compared to hydrogen generation. This is a general observation for any gold electrode.[20,21,23−25]

The FE(CO) for the three electrodes is shown in Figure 2D. The three different regimes observed in FE(CO) represent a trend that is typically observed for CDR on gold electrodes:[20−22,25,36,37] namely, as the applied potential is increased cathodically, the FE(CO) rises (regime I), reaches a maximum (regime II), and then decreases (regime III). In the low overpotential window of regime I, HER and CDR are similar after which CDR begins to dominate, thus causing a rapid rise in FE(CO). In regime II, FE(CO) reaches a maximal value above 80% for both the leaf and wire electrodes, whereas it plateaus at 40% for the film electrode. Normalization of the current densities by the electroactive surface area clearly shows that the primary reason for the discrepancy in FE(CO) is that HER reactivity is higher on the flat film electrode as compared to the leaf and wire electrodes (Figure 3A), whereas the CO_2 intrinsic reactivity is quite similar on all three electrodes (Figure 3B). In regime III at high overpotential, FE(CO) decreases as a consequence of CO partial current density leveling off with an attendant increase in HER activity.

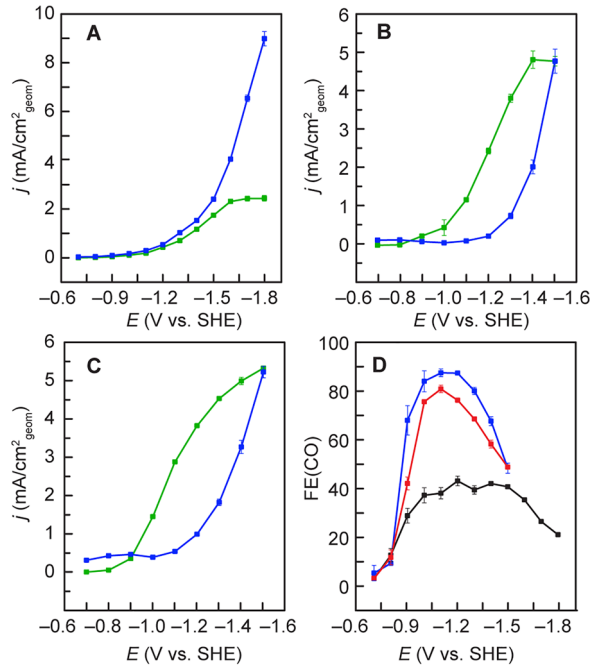

Figure 2. Partial current densities for CO (green) and H_2 (blue) production obtained by electrolysis of a 0.1 $NaHCO_3$ and 0.5 $NaClO_4$ solution under a CO_2 atmosphere on the (A) film, (B) leaf, and (C) wire electrodes. (D) Faradaic efficiency for CO production on the film (black), leaf (blue), and wire (red) electrodes. Each data point is the average of three measurements, and error limits are within the represented point unless shown.

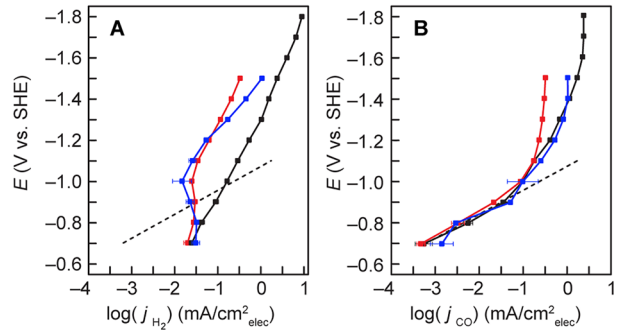

Figure 3. Partial current densities normalized by electrochemically active surface area for (A) H_2 and (B) CO on a film (black), leaf (blue), and wire (red) electrode. Predicted Tafel plots for (A) direct reduction of H_3O^+ on gold and (B) linear Tafel plot of 120 mV are shown by the dashed lines.

The general trends in FE(CO) and current density characteristics of the three regimes shown in Figure 2 are now analyzed, and a comprehensive kinetic analysis is developed in light of the mass transport and homogeneous solution reactions of species shown in Table 1.

DISCUSSION

CDR on gold electrodes in the commonly used $NaHCO_3$ electrolyte generates predominantly CO and H_2. Although the formation of other products has been reported,[37] their corresponding faradaic efficiencies are insignificant. As summarized in Table 1 for CDR in $NaHCO_3$ solution, several

DOI: 10.1021/acscentsci.9b00302
ACS Cent. Sci. 2019, 5, 1097−1105

distinct reactions should in principle be considered due to the presence of a priori competent proton donors in CO_2 saturated $NaHCO_3$ solutions, namely, H_3O^+, H_2CO_3, HCO_3^-, and H_2O. Different proton donors may give rise to one CO or one H_2 molecule (Table 2). Moreover, the reactions in Table 1 can

Table 2. Electrochemical Reactions

reaction	E^0 (V vs SHE)
CDR	
$CO_2 + 2\ e^- + 2\ H_3O^+ \rightleftharpoons CO + 3\ H_2O$	−0.11
$CO_2 + 2\ e^- + 2\ H_2CO_3 \rightleftharpoons CO + 2\ HCO_3^- + H_2O$	−0.32
$CO_2 + 2\ e^- + 2\ HCO_3^- \rightleftharpoons CO + 2\ CO_3^{2-} + H_2O$	−0.72
$CO_2 + 2\ e^- + H_2O \rightleftharpoons CO + 2\ HO^-$	−0.94
HER	
$2\ H_3O^+ + 2\ e^- \rightleftharpoons H_2 + 2\ H_2O$	0
$2\ H_2CO_3 + 2\ e^- \rightleftharpoons H_2 + 2\ HCO_3^-$	−0.21
$2\ HCO_3^- + 2\ e^- \rightleftharpoons H_2 + 2\ CO_3^{2-}$	−0.61
$2\ H_2O + 2\ e^- \rightleftharpoons H_2 + 2\ HO^-$	−0.83

alter the concentration of substrates proximate to the electrode for both CDR and HER. Therefore, all reactions displayed in Tables 1 and 2 must be considered to obtain an accurate depiction of CDR and HER.

The two electrochemical reactions, CDR and HER, are coupled because both involve a proton source as a (co)-substrate (Table 2). We note that the rate laws for both CDR and HER are insufficient to completely characterize the system and hence predict FE(CO). Indeed, proton transfers may not be involved in the rate-determining step for CDR, and therefore the rate of consumption of individual proton donors at the electrode surface is unknown and may a priori influence the current densities. Previous attempts at such modeling have been performed under the assumption that water is the sole proton donor.[16,32,38−40] In our analysis, we show that the output of the modeling is not dependent on the proton donor identity (vide infra).

The observed general trends reflected in Figure 2 are representative of the behavior of CDR on gold electrodes, regardless of different gold morphologies. With appropriate consideration of mass transport conditions and homogeneous reactions, comparative analysis of partial current densities (for HER and CDR) and their corresponding kinetics on the various electrodes offers the opportunity to gain insight into the factors governing intrinsic catalyst activity and FE(CO). To this end, steady-state, potentiostatic current densities are analyzed assuming that all three electrodes behave under the condition of the linear diffusion of species with a fixed diffusion layer thickness δ = 190 μm. This assumption is justified by the observation that the size of the diffusion layer is much larger than the depth of the catalyst layer. The roughness of the electrode is thus taken into consideration as a multiplicative enhancement factor (R_f) in the partial current densities of interfacial reactions.

At low overpotential (E > −0.9 V vs SHE), CO partial current is proportional to the electrochemical surface area and leads to a 120 mV slope Tafel plot (Figure 3B). This result conforms with previously reported studies,[28,41] though there have been isolated reports of 60 mV Tafel slopes at low overpotential.[29] A Tafel slope of 120 mV indicates that electron transfer from the electrode is rate limiting and that mass transport of species is not involved in the rate law.[42] We note that a formal kinetics analysis of the Volmer−Heyrovsky type reaction scheme will introduce curvature in Tafel plots at low overpotential as the Volmer step may approach reversibility.[43] As a consequence, the Tafel slope may decrease at low overpotential, below 120 mV, accounting for the apparent discrepancy of 60 mV Tafel slopes for CDR on gold. Our results are consistent with the proposal that CDR is governed by initial electron transfer,[26]

$$CO_2 + e^- \rightleftharpoons (CO_2^{\bullet -})_{ads} \quad (1)$$

with an attendant rate law that is independent of the proton donor,

$$i_{CO} = 2FS_{geom}R_f k^0_{CO_2}[CO_2]_{x=0} \exp\left(\frac{\alpha_C FE}{RT}\right) \quad (2)$$

where F is the Faraday, T is the temperature, and $[CO_2]_{x=0}$ is the concentration of CO_2 at the electrode surface. For E > −0.9 V vs SHE, $[CO_2]_{x=0}$ is equal to the bulk concentration of CO_2. α_C is the transfer coefficient equal to 0.5 as derived from the 120 mV Tafel slope. $k_{CO_2}^0$ is the intrinsic rate constant for CO_2 reduction on gold of 8.2 × 10^{-14} cm s^{-1}, which is determined from the fitting of the linear part of Tafel plot shown in Figure 3B with eq 2. Note that $k_{CO_2}^0$ is not the standard rate constant for CO_2 reduction on gold, i.e., the rate constant at a potential equal to the unknown standard potential of $CO_2/(CO_2^{\bullet -})_{ads}$ couple but is the value of the rate constant at a potential equal to the reference electrode potential (SHE). On the basis of a previous investigation of the reduction of strong acid on gold,[44] we estimate an intrinsic rate constant for HER to be $k_{H_3O^+}^0$ = 2.17 × 10^{-8} cm s^{-1}, which leads to a Tafel plot shown by the dashed line in Figure 3A. Interestingly, the Tafel slope for HER on gold with H_3O^+ as a substrate, assuming mass transport is not limiting owing to complete replenishment of H_3O^+ via chemical steps, is similar to the Tafel slope for CO production (dashed line in Figure 3B). However, the poor agreement between the experimentally observed data and the calculated Tafel slope (Figure 3A) suggests that H_3O^+ is not the proton source for HER. The small FE(CO) at low overpotential is thus not a consequence of efficient HER but rather is due to sluggish initial electron transfer to CO_2 together with H_3O^+ not being the proton donor for HER at the electrode surface. That H_2 partial current exhibits a shallow dependence on potential (Figure 3A) and is proportional to S_{elec} (Figure S7) leads to the conclusion that HER is kinetically controlled by a chemical step at the electrode surface prior to any electrochemical step. Indeed, any potential independent kinetics that are controlled by mass transport, whether the species is provided from the bulk or by a homogeneous chemical step, would lead to a current that is proportional to S_{geom} and independent of R_f. Alternatively, the current of a process involving an electron transfer as the rate-determining step or prior to the rate-determining step would be potential dependent. We propose that the chemical step governing HER at low overpotential is a rate-determining acid (HA) dissociation on the surface, followed by a fast reduction of the adsorbed proton (Scheme 1). A priori HA can be any of the four competent proton donors provided that they are replenished faster than the surface dissociation (rds, Scheme 1) step that corresponds to an observed limiting current density of ≤0.5 mA cm^{-2} (see Figure 2). Therefore, the proton donor concentration must be large enough such that the diffusion limiting current must be greater than 0.5 mA cm^{-2}. Because the concentrations of H_2O and HCO_3^- are large, the issue of

DOI: 10.1021/acscentsci.9b00302
ACS Cent. Sci. 2019, 5, 1097−1105

Scheme 1. Proposed HER Process at Low Overpotential

$$AH \overset{\text{fast}}{\rightleftharpoons} AH_{ads}$$
$$AH_{ads} \overset{\text{rds}}{\longrightarrow} A^-_{ads} + H^+_{ads}$$
$$2\,H^+_{ads} + 2\,e^- \overset{\text{fast}}{\longrightarrow} H_2$$

replenishing the proton donor at rates in excess of surface dissociation of HA only applies if H_3O^+ and H_2CO_3 are proton donors. To assess the viability of H_3O^+ and H_2CO_3 as proton donors for HER, simulations (see Supporting Information) were performed assuming fast kinetics for HER and the reactions and substrate concentrations listed in the footnote in Table 1. We find that H_2CO_3 and H_3O^+, as substrates for HER, furnish current densities of 1 mA cm^{-2} and 0.06 mA cm^{-2}, respectively, as a result of limiting substrate replenishment. Consequently, we can reasonably exclude hydronium as a substrate for HER in regime I but not H_2CO_3, which is thus a competent HER substrate together with HCO_3^- and H_2O. Although initially small, the CDR current density in regime I increases more quickly (120 mV Tafel slope) than HER (almost constant current density), and therefore FE(CO) rises rapidly.

In regime II ($-1.2 < E < -0.9$ V vs SHE), FE(CO) attains a maximum value of ~80% for both wire and leaf electrodes and ~40% for the film electrode owing to HER displaying a larger Tafel slope (Figure 3A) than CDR (Figure 3B). An increase of the CDR Tafel slope from the linear 120 mV slope at low overpotential is observed due to a decrease of $[CO_2]_{x=0}$ relative to its bulk value $[CO_2]_{x=\infty}$ (electrode deactivation was not observed, and CO adsorption on the electrode was not impactful (Figure S3) as it has been shown there is insignificant inhibition of active sites by CO[26]). Under the assumption that CO_2 is only consumed at the electrode surface, the CO current density should follow the Koutecky–Levich expression:

$$\frac{S_{geom}}{i_{CO}} = \frac{1}{2FR_f k^0_{CO_2}[CO_2]_{x=0}\exp\left(-\frac{\alpha_C FE}{RT}\right)} + \frac{\delta}{2FD[CO_2]_{x=\infty}} \quad (3)$$

Figure 4A,B indicates that the Koutecky–Levich expression, which describes the kinetic activity of CDR and mass transport of CO_2, does not account for the observed increase in Tafel slope when current densities > ~0.1 mA cm^{-2} are reached. The deviation of the observed data from the simulations predicted by eq 3 indicate that homogeneous reactions corresponding to CO_2 consumption play an important role in determining the CO current density. In the case of leaf and wire electrodes, the homogeneous consumption of CO_2 may be triggered by the production of base, particularly the OH^- hydration reaction shown in Table 1. Predictions of the effect of homogeneous reactions on CO production rely on numerical simulation due to the nonlinear character of the reaction-diffusion equation. The simulations represented by Figure 4C,D (see Supporting Information for details) were performed for both the leaf and wire electrodes based on the rate law described by eq 2) for CO production. As mentioned, the nature of the proton donor for CDR, and thus of the conjugate base, cannot be obtained from the rate law as protonation occurs beyond the rate-determining step. Therefore, simulations were performed considering H_2O and HCO_3^- as the proton donors, owing to their high concentrations (the concentration of H_2CO_3 is too low to maintain the current densities observed in this regime). In either case, the same current density is obtained indicating a fast buffering process of bicarbonate. The inclusion of the homogeneous reactions modifies Koutecky–Levich behavior to better fit the data (Figure 4C,D) owing to consumption of CO_2 through hydration processes, especially for reaction of CO_2 with OH^- which is 10 orders of magnitude faster than hydration by H_2O and is irreversible. In Figure 4C,D, the current density for CO production is well simulated at low overpotential (no effect of mass transport and homogeneous reactions, $[CO_2]_{x=0} = [CO_2]_{x=\infty}$) as well as at high overpotential where CO_2 reduction kinetics are overwhelmed by both mass transport and homogeneous reactions. However, at intermediate overpotential, the simulated CO current density is higher than that observed experimentally. We propose that this discrepancy between simulation and experiment arises from a breakdown of the Volmer expression (eq 2) over the entire potential range. Indeed, the low HER contribution for $E > -1.3$ V vs SHE on both the leaf and wire electrodes offers a unique opportunity to investigate the intrinsic reactivity of CO_2 on gold over a large potential range (700 mV), provided that mass transport and the homogeneous reactions are appropriately considered as is done in our simulations. We thus performed simulations (see Supporting Information) in which an apparent rate constant $k^{ap}_{f,CO_2}(E)$ as defined by eq 4 was adjusted at each potential to match experimentally measured currents, i_{CO},

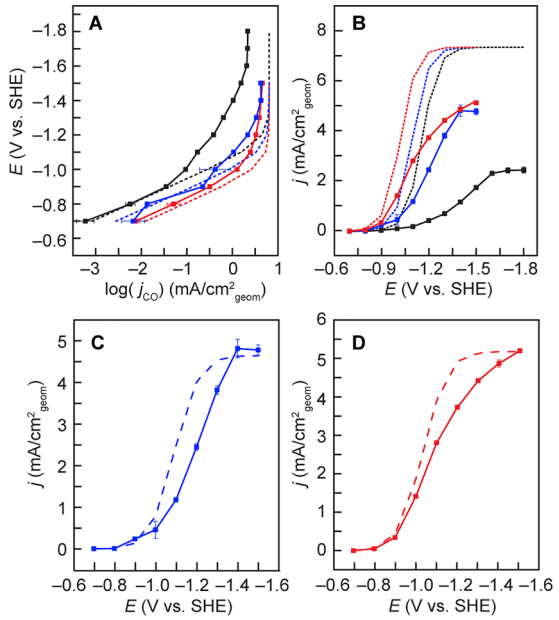

Figure 4. (A) Partial current densities for CO production, normalized by geometric surface area, on a film (black), a leaf (blue), and a wire (red) electrode. Dashed lines show the simulation according to the Koutecky–Levich expression, eq 3. (B) Data from (A) replotted to show the deviation between experimental data and Koutecky–Levich simulations. Koutecky–Levich simulation with concentrations of species modified owing to homogeneous reactions for the (C) leaf electrode and (D) the wire electrode. Dashed lines show simulations of $j_{CO} = i_{CO}/S$ for the using eq 2 with consideration of mass transport and homogeneous reactions.

DOI: 10.1021/acscentsci.9b00302
ACS Cent. Sci. 2019, 5, 1097–1105

$$i_{CO} = 2FS_{geom}R_f k^{ap}_{f,CO_2}(E)[CO_2]_{x=0} \quad (4)$$

No assumption is made with regard to the activation-driving force relationship for the rate-determining step, which is the initial electron transfer as described by reaction 1. Note that we assume that the number of free active sites on the surface remains large (relative to the total number of active sites) and constant over the entire range of potential, a condition readily achieved with the rate-determining step being initial electron transfer. In fact, kinetic interference by a chemical step following the initial electron transfer cannot account for the discrepancy between simulation and experiment at intermediate potentials (Figure S8) (see Supporting Information for details). We observe that both the leaf and wire electrodes display similar apparent rate constants (Figure 5), and a

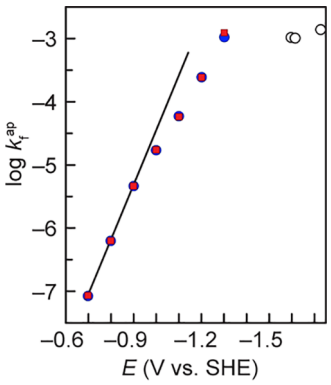

Figure 5. Apparent rate constant for CO_2 reduction on leaf (●, blue) and wire (■, red) electrodes as a function of potential. The line is generated from the linear Volmer law with $\alpha_C = 0.5$. The circles (○) are the rate constant for CO_2 reduction on a gold electrode in DMSO reported in ref 45.

notable deviation is observed from the linear Volmer law at high driving force. Several possibilities may explain such behavior: (i) the inner sphere electron transfer rate is dependent on the local acid−base environment and the observed potential dependence is actually a pH-dependence, (ii) the inner sphere electron transfer is not a single elementary step, and a potential-dependent preassociation of CO_2 with the surface occurs, or (iii) the intrinsic properties of surface associative inner sphere electron transfer are not accounted for by theory. Possibility (i) is ruled out by the observation that similar apparent rate constants are observed for both the leaf and wire electrodes, whereas the simulated surface pHs at each electrode are different (Figure S9). Although it is difficult to discern between (ii) and (iii), the deviation is relegated to the inner sphere electron transfer and thus represents, to the best of our knowledge, the first observation of a nonlinear activation-driving force relationship for an inner sphere electron transfer with a surface association. Interestingly, the rate constant for CO_2 reduction measured in DMSO[45] agrees with our data extrapolated to the asymptotic value of Figure 5. We observe that the apparent activation-driving force relationship exhibits a striking similarity with outer sphere electron transfers at the metal−electrolyte interface for which such an asymptotic limit is predicted as a consequence of the distribution of electronic states in the electrode.[46]

The dominance of CDR over HER in regime II is a consequence of lower HER activity coupled to increasing CDR activity. FE(CO) is low and constant on the film due to the interplay of two phenomena: an apparent high Tafel slope due to CO production that is partially limited by mass transport and homogeneous reactions, and H_2 production occurs with a similarly high Tafel slope (400 mV). The onset of HER occurs on the wire and leaf electrodes at higher overpotential ($E < -1$ V vs SHE), furnishing a higher maximum FE(CO). According to previous reports,[26] this onset of HER is attributed to the direct reduction of HCO_3^-. We note however that the elementary process for HCO_3^- reduction cannot be simply described by a Volmer rate-determining step since the reported reaction order is lower than unity.[26] Additionally, the apparent Tafel slope is very high and would imply a transfer coefficient as small as 0.145 with no theoretical justification. Considering eq 5 as an ad hoc apparent rate law for HER,

$$i_{H_2} = 2FS_{geom}R_f k^{ap}_{HCO_3^-} \exp\left(-\frac{\alpha^{ap}_H FE}{RT}\right)[HCO_3^-]_{x=0} \quad (5)$$

where $\alpha^{ap}_H = 0.145$ and $k^{ap}_{HCO_3^-}$ is the apparent rate constant for direct HCO_3^- reduction on a gold film electrode, simulations were performed (see Supporting Information for details). $k^{ap}_{HCO_3^-}$ was evaluated as 2.25×10^{-8} cm^2 s^{-1} and both i_{CO} and i_{H_2}, and accordingly FE(CO), are well reproduced up to −1.1 V vs SHE (Figure S10). At higher overpotential, the experimental i_{CO} is smaller than its simulated value, even with the inclusion of the deviation of the CO_2 reduction activation-driving force relation from the Volmer law, possibly due to a partial inhibition of CO_2 reduction by HER. Such a phenomenon is not observed for leaf and wires electrodes due to much lower HER activity.

As the potential is increased more negatively beyond −1.2 V vs SHE (regime III), FE(CO) drops for both leaf and wire electrodes and for the film electrode at slightly higher overpotential. This decrease of FE(CO) is a consequence of a simultaneous increase in HER and leveling of CDR. The increase of HER can be attributed to the direct reduction of HCO_3^-, though there may also be some contribution to HER arising from the direct reduction of H_2O. As outlined for regime II, the limiting CO current density reflects that CDR is no longer controlled by CO_2 activation but by a combination of CO_2 diffusion and its homogeneous consumption by the hydration reaction with hydroxide ions produced via both HER and CDR, either directly or indirectly.

Several consequences emerge from our analysis with regard to the conditions required to reach high current densities (above 150 mA cm^2) as is desired for practical applications.[47,48] First, as long recognized,[49] the mass transport required to support high current densities can be achieved by a gas diffusion electrode (GDE)[50] or an equivalent three-phase interface.[51] Mass transport may also be accelerated by the formation of small bubbles on nanostructured surfaces.[52] On the basis of the results of Figure 2 and attendant analysis, the potential on a gold cathode should be maintained positive of −1.3 V vs SHE to attain high FE(CO). The measured value of $k^{ap}{}_{CO_2}(E)$ at this potential in conjunction with the consideration that $[CO_2] = 0.038$ M over the entire active surface area (we note that although CO_2 is supplied to gas diffusion electrodes from a gas phase, the reactant at the catalyst surface is dissolved CO_2), application of eq 4 indicates that the electrode roughness ($R_f = S_{elec}/S$) should be higher than 20 to reach 150 mA cm^2. Second, such a high roughness must be obtained for a thin porous catalyst layer so as to maintain

DOI: 10.1021/acscentsci.9b00302
ACS Cent. Sci. 2019, 5, 1097−1105

$[CO_2]$ = 0.038 M over the entire active surface area due to the problematic production of hydroxide anions by CDR that readily react with CO_2 and accelerate CO_2 depletion within the catalyst layer. A simplified modeling (see Supporting Information) indicates that the catalyst layer has to be on the order of a few micrometers (Scheme 2). The formation of

Scheme 2. Gas Diffusion Electrode and Schematic CO_2 Concentration

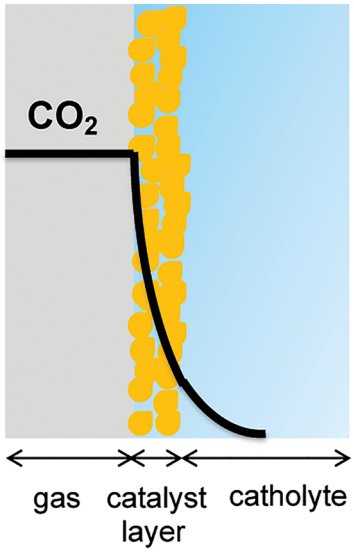

such concentration gradients within the electrode nanostructures, even for the 10 μm depth of the wire electrode described here, is not achieved because of (i) small observed current densities and (ii) determination of CO_2 concentration at the catalyst surface by homogeneous reactions and mass transport outside the electrode nanostructure. Third, attempts have been made to suppress HER at high current densities by performing CDR in basic solution, thereby precluding direct reduction of bicarbonate.[53−55] We again emphasize that engineering the catalyst layer is crucial because CO_2 penetration in basic media is limited by rapid formation of carbonate leading to a CO_2 depletion layer that can be roughly evaluated to be on the order of $\sqrt{D_{CO_2}/k_{OH^-}[OH^-]} \approx 1\mu m$ in a 1 M hydroxide solution (k_{OH} is the rate constant for CO_2 reaction with hydroxide ion). Finally, we note that this approach to use basic solution to avoid bicarbonate drastically reduces the carbon efficiency of CDR owing to the hydration reaction listed in Table 1. Thus, while high FE(CO) may be achieved by this approach, the CO_2 conversion efficiency is quite low, and such practical applications of CDR must therefore consider additional practical complexities (and associated costs) with separating CO_3^{2-} and regenerating CO_2.

CONCLUSION

We investigate the CDR selectivity on gold electrodes with very different morphologies. A comprehensive kinetics model, with the inclusion of mass transport and the role of homogeneous reactions, allows the intrinsic activity of the catalyst toward CDR vs HER to be defined. This analysis uncovers an activation-driving force relationship over a large applied potential window that deviates from expected Volmer Law behavior. Thus, owing to this deviation, catalyst behavior cannot be studied exclusively at low overpotential and then extrapolated to higher overpotentials. The general trends observed in FE(CO) are explained by the limiting roles of mass transport and homogeneous reactions, which arise upon reaching high current densities in the system. Crucially, OH^- generated via CDR and HER results in nonproductive consumption of CO_2 local to the electrode. As such, efforts to mitigate the impact of mass transport using GDEs to achieve high current density must incude the important consideration of homogeneous CO_2 consumption in regard to the mass balance of CO_2 in the system.

ASSOCIATED CONTENT

Supporting Information

The Supporting Information is available free of charge on the ACS Publications website at DOI: 10.1021/acscentsci.9b00302.

Experimental details, electrochemical surface area, diffusion layer thickness, simulations (PDF)

AUTHOR INFORMATION

Corresponding Authors

*(C.C.) E-mail: cyrille.costentin@univ-paris-diderot.fr.
*(D.G.N.) E-mail: dnocera@fas.harvard.edu.

ORCID

Cyrille Costentin: 0000-0002-7098-3132
Daniel G. Nocera: 0000-0001-5055-320X

Notes

The authors declare no competing financial interest.

ACKNOWLEDGMENTS

This material is based upon work supported under the Solar Photochemistry Program of the Chemical Sciences, Geosciences and Biosciences Division, Office of Basic Energy Sciences of the U.S. Department of Energy DE-SC0017619.

REFERENCES

(1) Lewis, N. S.; Nocera, D. G. Powering the Planet: Chemical Challenges in Solar Energy Utilization. *Proc. Natl. Acad. Sci. U. S. A.* **2006**, *103*, 15729−15735.
(2) Nocera, D. G. "Fast Food" Energy. *Energy Environ. Sci.* **2010**, *3*, 993−995.
(3) Chu, S.; Majumdar, A. Opportunities and Challenges for a Sustainable Energy Future. *Nature* **2012**, *488*, 294−303.
(4) Lewis, N. S.; Nocera, D. G. The Solar Opportunity. *Bridge* **2015**, *46*, 41−47.
(5) Cook, T. R.; Dogutan, D. K.; Reece, S. Y.; Surendranath, Y.; Teets, T. S.; Nocera, D. G. Solar Energy Supply and Storage for the Legacy and Nonlegacy Worlds. *Chem. Rev.* **2010**, *110*, 6474−6502.
(6) Arakawa, H.; Aresta, M.; Armor, J. N.; Barteau, M. A.; Beckman, E. J.; Bell, A. T.; Bercaw, J. E.; Creutz, C.; Dinjus, E.; Dixon, D. A.; Domen, K.; DuBois, D. L.; Eckert, J.; Fujita, E.; Gibson, D. H.; Goddard, W. A.; Goodman, D. W.; Keller, J.; Kubas, G. J.; Kung, H. H.; Lyons, J. E.; Manzer, L. E.; Marks, T. J.; Morokuma, K.; Nicholas, K. M.; Periana, R.; Que, L.; Rostrup-Nielson, J.; Sachtler, W. M. H.; Schmidt, L. D.; Sen, A.; Somorjai, G. A.; Stair, P. C.; Stults, B. R.; Tumas, W. Catalysis Research of Relevance to Carbon Management: Progress, Challenges, and Opportunities. *Chem. Rev.* **2001**, *101*, 953−996.
(7) Costentin, C.; Robert, M.; Savéant, J.-M. Catalysis of the Electrochemical Reduction of Carbon Dioxide. *Chem. Soc. Rev.* **2013**, *42*, 2423−2436.
(8) Azcarate, I.; Costentin, C.; Robert, M.; Savéant, J.-M. Through-Space Charge Interaction Substituent Effects in Molecular Catalysis Leading to the Design of the Most Efficient Catalyst of CO_2-to-CO

Electrochemical Conversion. *J. Am. Chem. Soc.* **2016**, *138*, 16639−16644.
(9) Kang, P.; Cheng, C.; Chen, Z.; Schauer, C. K.; Meyer, T. J.; Brookhart, M. Selective Electrocatalytic Reduction of CO_2 to Formate by Water-Stable Iridium Dihydride Pincer Complexes. *J. Am. Chem. Soc.* **2012**, *134*, 5500−5503.
(10) Sun, C.; Gobetto, R.; Nervi, C. Recent Advances in Catalytic CO_2 Reduction by Organometal Complexes Anchored on Modified Electrodes. *New J. Chem.* **2016**, *40*, 5656−5661.
(11) Li, C.; Kanan, M. W. CO_2 Reduction at Low Overpotential on Cu Electrodes Resulting from the Reduction of Thick Cu_2O Films. *J. Am. Chem. Soc.* **2012**, *134*, 7231−7234.
(12) Kortlever, R.; Shen, J.; Schouten, K. J. P.; Calle-Vallejo, F.; Koper, M. T. M. Catalysts and Reaction Pathways for the Electrochemical Reduction of Carbon Dioxide. *J. Phys. Chem. Lett.* **2015**, *6*, 4073−4082.
(13) Kwon, Y.; Lum, Y.; Clark, E. L.; Ager, J. W.; Bell, A. T. CO_2 Electroreduction with Enhanced Ethylene and Ethanol Selectivity by Nanostructuring Polycrystalline Copper. *ChemElectroChem* **2016**, *3*, 1012−1019.
(14) Kim, D.; Resasco, J.; Yu, Y.; Asiri, A. M.; Yang, P. Synergistic Geometric and Electronic Effects for Electrochemical Reduction of Carbon Dioxide using Gold-Copper Bimetallic Nanoparticles. *Nat. Commun.* **2014**, *5*, 4948/1−8.
(15) Clark, E. L.; Hahn, C.; Jaramillo, T. F.; Bell, A. T. Electrochemical CO_2 Reduction over Compressively Strained CuAg Surface Alloys with Enhanced Multi-Carbon Oxygenated Selectivity. *J. Am. Chem. Soc.* **2017**, *139*, 15848−15857.
(16) Dinh, C.-T.; Burdyny, T.; Kibria, M. G.; Seifitokaldani, A.; Gabardo, C. M.; Garcia de Arquer, F. P.; Kiani, A.; Edwards, J. P.; De Luna, P.; Bushuyev, O.; Zou, C.; Quintero-Bermudez, R.; Pang, Y.; Sinton, D.; Sargent, E. H. CO_2 Electroreduction to Ethylene via Hydroxide-Mediated Copper Catalysis at an Abrupt Interface. *Science* **2018**, *360*, 783−787.
(17) Lee, C. H.; Kanan, M. W. Controlling H^+ vs. CO_2 Reduction Selectivity on Pb Electrodes. *ACS Catal.* **2015**, *5*, 465−469.
(18) Lu, Q.; Rosen, J.; Zhou, Y.; Hutchings, G. S.; Kimmel, Y. C.; Jiao, F.; Chen, J. G. A Selective and Efficient Electrocatalyst for Carbon Dioxide Reduction. *Nat. Commun.* **2014**, *5*, 3242/1−6.
(19) Chen, Y.; Li, C. W.; Kanan, M. W. Aqueous CO_2 Reduction at Very Low Overpotential on Oxide-Derived Au Nanoparticles. *J. Am. Chem. Soc.* **2012**, *134*, 19969−19972.
(20) Hall, A. S.; Yoon, Y.; Wuttig, A.; Surendranath, Y. Mesostructure-Induced Selectivity in CO_2 Reduction Catalysis. *J. Am. Chem. Soc.* **2015**, *137*, 14834−14837.
(21) Zhu, W.; Michalsky, R.; Metin, Ö.; Lv, H.; Guo, S.; Wright, C. J.; Sun, X.; Peterson, A. A.; Sun, S. Monodisperse Au Nanoparticles for Selective Electrocatalytic Reduction of CO_2 to CO. *J. Am. Chem. Soc.* **2013**, *135*, 16833−16836.
(22) Feng, X.; Jiang, K.; Fan, S.; Kanan, M. W. Grain-Boundary-Dependent CO_2 Electroreduction Activity. *J. Am. Chem. Soc.* **2015**, *137*, 4606−4609.
(23) Zhu, W.; Zhang, Y.-J.; Zhang, H.; Lv, H.; Li, Q.; Michalsky, R.; Peterson, A. A.; Sun, S. Active and Selective Conversion of CO_2 to CO on Ultrathin Au Nanowires. *J. Am. Chem. Soc.* **2014**, *136*, 16132−16135.
(24) Liu, M.; Pang, Y.; Zhang, B.; De Luna, P.; Voznyy, O.; Xu, J.; Zheng, X.; Dinh, C. T.; Fan, F.; Cao, C.; de Arquer, F. P. G.; Safaei, T. S.; Mepham, A.; Klinkova, A.; Kumacheva, E.; Filleter, T.; Sinton, D.; Kelley, S. O.; Sargent, E. H. Enhanced Electrocatalytic CO_2 reduction via Field-Induced Reagent Concentration. *Nature* **2016**, *537*, 382−386.
(25) Lee, H.-Y.; Yang, K. D.; Yoon, S. M.; Ahn, H.-Y.; Lee, Y. Y.; Chang, H.; Jeong, D. H.; Lee, Y.-S.; Kim, M. Y.; Nam, K. T. Concave Rhombic Dodecahedral Au Nanocatalyst with Multiple High-Index Facets for CO_2 Reduction. *ACS Nano* **2015**, *9*, 8384−8393.
(26) Wuttig, A.; Yaguchi, M.; Motobayashi, K.; Osawa, M.; Surendranath, Y. Inhibited Proton Transfer Enhances Au-Catalyzed CO_2-to-Fuels Selectivity. *Proc. Natl. Acad. Sci. U. S. A.* **2016**, *113*, E4585−E4593.
(27) Dunwell, M.; Lu, Q.; Heyes, J. M.; Rosen, J.; Chen, J. G.; Yan, Y.; Jiao, F.; Xu, B. The Central Role of Bicarbonate in the Electrochemical Reduction Reduction of Carbon Dioxide on Gold. *J. Am. Chem. Soc.* **2017**, *139*, 3774−3783.
(28) Wuttig, A.; Yoon, Y.; Ryu, J.; Surendranath, Y. Bicarbonate is Not a General Acid in Au-Catalyzed CO_2 Electroreduction. *J. Am. Chem. Soc.* **2017**, *139*, 17109−17113.
(29) Dunwell, M.; Luc, W.; Yan, Y.; Jiao, F.; Xu, B. Understanding Surface-Mediated Electrochemical Reactions: CO_2 Reduction and Beyond. *ACS Catal.* **2018**, *8*, 8121−8129.
(30) Lee, C. W.; Cho, N. H.; Im, S. W.; Jee, M. S.; Hwang, Y. J.; Min, B. K.; Nam, K. T. New Challenges of Electrokinetic Studies in Investigating the Reaction Mechanism of Electrochemical CO_2 Reduction. *J. Mater. Chem. A* **2018**, *6*, 14043−14057.
(31) Clark, E. L.; Resasco, J.; Landers, A.; Lin, J.; Chung, L.-T.; Walton, A.; Hahn, C.; Jaramillo, T. F.; Bell, A. T. Standards and Protocols for Data Acquisition and Reporting for Studies of the Electrochemical Reduction of Carbon Dioxide. *ACS Catal.* **2018**, *8*, 6560−6570.
(32) Gupta, N.; Gattrell, M.; MacDougall, B. Calculation for the Cathode Surface Concentrations in the Electrochemical Reduction of CO_2 in $KHCO_3$ Solutions. *J. Appl. Electrochem.* **2006**, *36*, 161−172.
(33) Ho, C.; Sturtevant, J. M. The Kinetics of the Hydration of Carbon Dioxide at 25°. *J. Biol. Chem.* **1963**, *238*, 3499−3501.
(34) Pohorecki, R.; Moniuk, W. Kinetics of Reaction Between Carbon Dioxide and Hydroxyl Ions in Aqueous Electrolyte Solutions. *Chem. Eng. Sci.* **1988**, *43*, 1677−1684.
(35) Ozel, T.; Zhang, B. A.; Gao, R.; Day, R. W.; Lieber, C. M.; Nocera, D. G. Electrochemical Deposition of Conformal and Functional Layers on High Aspect Ration Silicon Micro/Nanowires. *Nano Lett.* **2017**, *17*, 4502−4507.
(36) Noda, H.; Ikeda, S.; Oda, Y.; Imai, K.; Maeda, M.; Ito, K. Electrochemical Reduction of Carbon Dioxide at Various Metal Electrodes in Aqueous Potassium Hydrogen Carbonate Solution. *Bull. Chem. Soc. Jpn.* **1990**, *63*, 2459−2462.
(37) Cave, E. R.; Montoya, J. H.; Kuhl, K. P.; Abram, D. N.; Hatsukade, T.; Shi, C.; Hahn, C.; Norskov, J. K.; Jaramillo, T. F. Electrochemical CO_2 Reduction on Au Surfaces: Mechanistic Aspects Regarding the Formation of Major and Minor Products. *Phys. Chem. Chem. Phys.* **2017**, *19*, 15856−15863.
(38) Singh, M. R.; Clark, E. L.; Bell, A. T. Effects of Electrolyte, Catalyst, and Membrane Composition and Operating Conditions on the Performance of Solar-Driven Electrochemical Reduction of Carbon Dioxide. *Phys. Chem. Chem. Phys.* **2015**, *17*, 18924−18936.
(39) Delacourt, C.; Ridgway, P. L.; Newman, J. Mathematical Modeling of CO_2 Reduction to CO in Aqueous Electrolytes. *J. Electrochem. Soc.* **2010**, *157*, B1902−B1910.
(40) Resasco, J.; Lum, Y.; Clark, E. L.; Zeledon, J. Z.; Bell, A. T. Effects of Anion Identity and Concentration on Electrochemical Reduction of CO_2. *ChemElectroChem* **2018**, *5*, 1064−1072.
(41) Hori, Y.; Murata, A.; Kikuchi, K.; Suzuki, S. Electrochemical Reduction of Carbon Dioxide to Carbon Monoxide at a Gold Electrode in Aqueous Potassium Hydrogen Carbonate. *J. Chem. Soc., Chem. Commun.* **1987**, *10*, 728−729.
(42) Savéant, J.-M. Single Electron Transfer at an Electrode. In *Elements of Molecular and Biomolecular Electrochemistry: An Electrochemical Approach to Electron Transfer Chemistry*; Wiley: Hoboken, NJ, 2006; pp 1−75.
(43) Costentin, C.; Savéant, J.-M. Catalysis of Electrochemical Reactions by Surface-Actives Sites: Analyzing the Occurrence and Significance of Volcano Plots by Cyclic Voltammetry. *ACS Catal.* **2017**, *7*, 4876−4880.
(44) Brug, G. J.; Sluyters-Rehbach, M.; Sluyters, J. H.; Hemelin, A. The Kinetics of the Reduction of Protons at Polycrystalline and Monocrystalline Gold Electrodes. *J. Electroanal. Chem. Interfacial Electrochem.* **1984**, *181*, 245−266.

DOI: 10.1021/acscentsci.9b00302
ACS Cent. Sci. 2019, 5, 1097−1105

(45) Haynes, L. V.; Sawyer, D. T. Electrochemistry of Carbon Dioxide in Dimethyl Sulfoxide at Gold and Mercury Electrodes. *Anal. Chem.* **1967**, *39*, 332−338.
(46) Chidsey, C. E. D. Free Energy and Temperature Dependence of Electron Transfer at the Metal-Electrolyte Interface. *Science* **1991**, *251*, 919−922.
(47) Verma, S.; Kim, B.; Jhong, H.-R.; Ma, S.; Kenis, P. J. A. A Gross-Margin Model for Defining Technoeconomic Benchmarks in the Electroreduction of CO_2. *ChemSusChem* **2016**, *9*, 1972−1979.
(48) Chen, C.; Kotyk, J. F. K.; Sheehan, S. W. Progress toward Commercial Application of Electrochemical Dioxide Reduction. *Chem.* **2018**, *4*, 2571−2586.
(49) Dewulf, D. W.; Bard, A. J. The Electrochemical Reduction of CO_2 to CH_4 and C_2H_4 at Cu/Nafion Electrodes (Solid Polymer Electrolyte Structures). *Catal. Lett.* **1988**, *1*, 73−80.
(50) Weekes, D. M.; Salvatore, D. A.; Reyes, A.; Huang, A.; Berlinguette, C. P. Electrolytic CO_2 Reduction in a Flow Cell. *Acc. Chem. Res.* **2018**, *51*, 910−918.
(51) Li, J.; Chen, G.; Zhu, Y.; Liang, Z.; Pei, A.; Wu, C.-L.; Wang, H.; Lee, H. R.; Liu, K.; Chu, S.; Cui, Y. Efficient Electrocatalytic CO_2 Reduction on a Three-Phase Interface. *Nat. Catal* **2018**, *1*, 592−600.
(52) Burdyny, T.; Graham, P. J.; Pang, Y.; Dinh, C.-T.; Liu, M.; Sargent, E. H.; Sinton, D. Nanomorphology-Enhanced Gas-Evolution Intensifies CO_2 Reduction Electrochemistry. *ACS Sustainable Chem. Eng.* **2017**, *5*, 4031−4040.
(53) Verma, S.; Hamasaki, Y.; Kim, C.; Huang, W.; Lu, S.; Jhong, H-H. M.; Gewirth, A. A.; Fujigaya, T.; Nakashima, N.; Kenis, P. J. A. Insights in the Low Overpotential Electroreduction of CO_2 to CO on a Supported Gold Catalyst in an Alkaline Flow Electrolyser. *ACS Energy Lett.* **2018**, *3*, 193−198.
(54) Dinh, C.-T.; Garcia de Arquer, F. P.; Sinton, D.; Sargent, E. H. High Rate, Selective, and Stable Electroreduction of CO_2 to CO in Basic and Neutral Media. *ACS Energy Lett.* **2018**, *3*, 2835−2840.
(55) Gabardo, C. M.; Seifitokaldani, A.; Edwards, J. P.; Dinh, C.-T.; Burdyny, T.; Kibria, M. G.; O'Brien, C. P.; Sargent, E. H.; Sinton, D. Combined High Alkanity and Pressurization Enable Efficient CO_2 Electroreduction to CO. *Energy Environ. Sci.* **2018**, *11*, 2531−2539.

DOI: 10.1021/acscentsci.9b00302
ACS Cent. Sci. 2019, 5, 1097−1105